ACS APPLIED BIO MATERIALS

www.acsabm.org
Article

Ferritin Fused with MiniSOG for *In Vitro* Photodynamic Therapy

Narathip Naradun,[⊥] Piyasiri Chueakwon,[⊥] Anyanee Kamkaew, Kai-Yu Hsu, Man Nee Lee, Kantapat Chansaenpak, Yane-Shih Wang,* and Rung-Yi Lai*

Cite This: *ACS Appl. Bio Mater.* 2025, 8, 3909−3919

ABSTRACT: To avoid off-target effects, targeted cancer therapy offers a feasible alternative to traditional cancer therapies such as chemotherapy and radiotherapy. The human ferritin receptor (transferrin receptor, TfR1) is greatly overexpressed in several cancer types, including liver cancer. Therefore, human ferritin (HFn) has been used in drug encapsulation for targeted therapy. However, the drug encapsulation method is time-consuming and not applicable to all conditions. In this study, we effectively designed HFn fused with a photosensitizing protein called mini-singlet oxygen generator (miniSOG) to create HFn-miniSOG for targeted photodynamic therapy (PDT) applications. The fusion protein HFn-miniSOG self-assembled to form nanoparticles with an average size of 22.4 ± 1.3 nm and generated singlet oxygen ($^1O_2$) when activated by blue-light irradiation with Φ_Δ = 0.30. To demonstrate its targeted PDT capability, phototoxicity was assessed in HepG2 and HeLa cells with varying TfR1 expression levels. The viability of HepG2 cells was reduced by 63% after light irradiation, compared to 34% in HeLa cells, because HepG2 cells exhibit greater levels of TfR1. As a result, our study provides a straightforward approach for creating ALL-IN-ONE protein nanoparticles for targeted PDT applications.

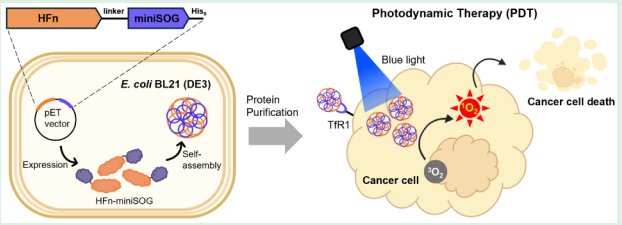

KEYWORDS: *ferritin, photodynamic therapy, photosensitizer protein, transferrin receptor, miniSOG, singlet oxygen, protein nanoparticles*

1. INTRODUCTION

Chemotherapy, radiation therapy, and surgical intervention are examples of first-line cancer therapies. However, they have not been able to completely eradicate the disease and have a number of substantial problems, including low tumor selectivity, systemic toxicity, off-target toxicity, multidrug resistance, and severe adverse health effects.[1] Targeted cancer therapy has recently emerged as a potential alternative to standard cancer treatments because of its superior therapeutic outcomes. However, only a few drugs are appropriate for this function. As a result, nanotechnology has evolved, presenting promising solutions to these challenges while also improving antitumor effectiveness.[2−6] Among them, protein nanoparticles have been intensively explored because of their natural availability and physiological compatibility.[7−11] Because proteins are biological molecules with unique properties, they can be applied to both materials science and biomedicine. In some cases, natural protein nanoparticles such as ferritins, encapsulins, and lumazine synthases perform highly specific biological activities.[12] By integrating functional protein domains, synthetic biology enables the engineering of natural protein nanoparticles with new features.

Ferritin is an ideal candidate for protein nanoparticles because of its unique properties such as great pH and temperature stability, uniform size, high biocompatibility, biodegradability, affordability, and the feasibility of large-scale production.[13−15] Ferritin can form a 12 nm-diameter 24-mer nanoparticle with an 8 nm-diameter hollow cavity. For this reason, ferritin nanoparticles have been developed to encapsulate anticancer drugs, bioactive nutrients, or enzymes for various applications.[16−20] In comparison to different nanodelivery strategies,[21] the advantage of utilizing ferritin as tumor-targeting nanocarriers is its intrinsic selectivity for TfR1, as well as the relative simplicity of administration.[22,23] TfR1 is overexpressed in various tumor types due to increased iron requirements for accelerated cell proliferation, although the level of overexpression varies by tumor type.[24] Differences in TfR1 expression across tumors are affected by tumor type and subtype, the tumor microenvironment, genetic and epigenetic alterations, and the impacts of therapies such as chemotherapy and radiotherapy. It was discovered that TfR1 is the receptor for HFn, and when HFn interacts with TfR1 on the cell membrane, it internalizes into the lysosome.[25] In 2012, the ability of HFn to specifically identify tumor tissues was demonstrated, proving HFn's potential as a targeted strategy in tumor diagnostics.[26] This discovery is significant because TfR1, which is widely known for its involvement in iron transport, is overexpressed in many cancer cells, making it an excellent

Received: January 15, 2025
Revised: April 11, 2025
Accepted: April 14, 2025
Published: April 22, 2025

https://doi.org/10.1021/acsabm.5c00098
ACS Appl. Bio Mater. 2025, 8, 3909−3919

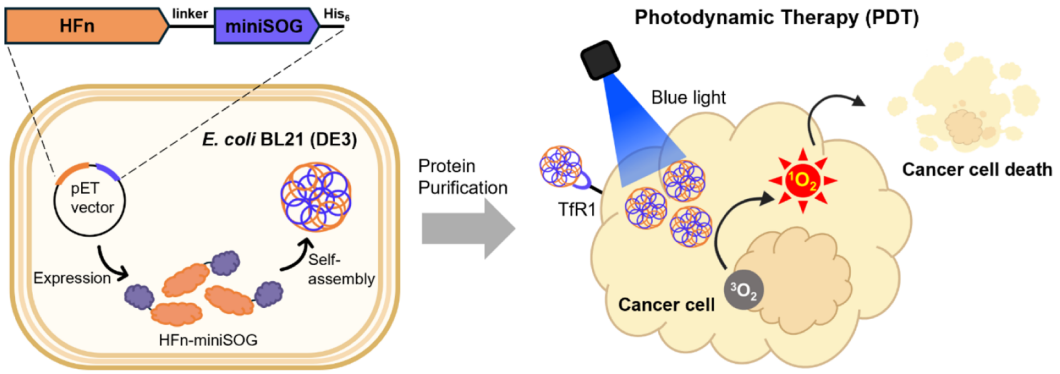

Figure 1. HFn-miniSOG nanoparticles for targeting cancer cells that overexpress TfR1. *E. coli* BL21(DE3) produced HFn-miniSOG nanoparticles. The purified protein nanoparticles were delivered into cancer cells via TfR1. Following light irradiation, the nanoparticles generated $^1O_2$ that eradicated cancer cells.

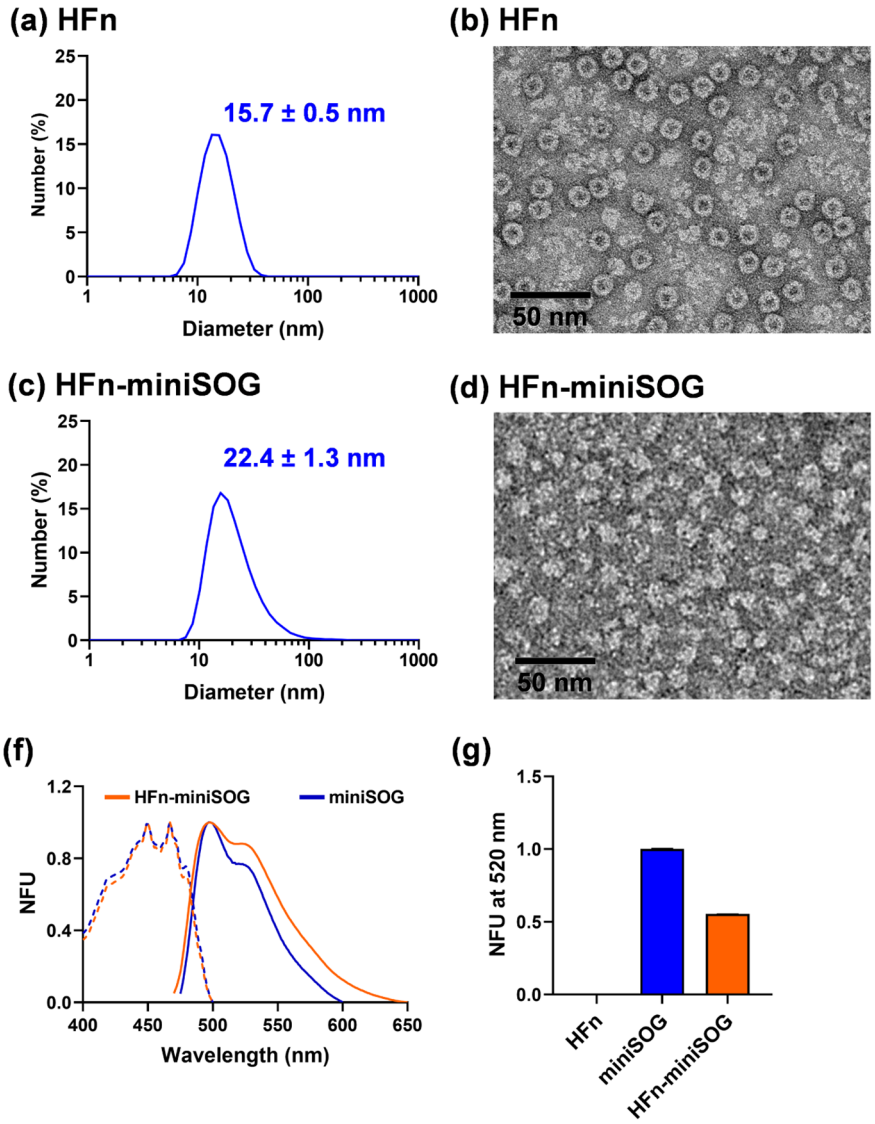

Figure 2. DLS analysis and TEM imaging of HFn nanoparticles (a ,b) and HFn-miniSOG nanoparticles (c,d). (f) Effect of encapsulation on the fluorescence excitation/emission spectra of miniSOG of HFn-miniSOG compared to miniSOG alone. Absorbance (dashed line) and fluorescence (solid line) spectra of HFn-miniSOG and miniSOG are given in normalized fluorescence units (NFU). (g) Fluorescence emission intensity (λ_{ex}/λ_{em} = 485/520 nm) of 10 μM HFn, miniSOG, and HFn-miniSOG. Each intensity was normalized to the highest fluorescence intensity value obtained in each data set. Error bars represent the mean ± standard deviation; n = 3 from three independent experiments.

https://doi.org/10.1021/acsabm.5c00098
ACS Appl. Bio Mater. 2025, 8, 3909−3919

target for tumor treatment and detection. As a result, it has been demonstrated that apoferritin-encapsulated Temozolomide and its analog are internalized via TfR1-mediated endocytosis, promoting brain cancer cell uptake and thereby improving therapeutic efficacy.[27] A similar method using apoferritin to encapsulate Jerantinine A was applied in breast cancer treatment.[28]

While chemotherapy remains an established cancer treatment, PDT has emerged as a promising alternative. PDT employs light to activate a photosensitizer (PS), which transforms molecular oxygen into reactive oxygen species (ROS). This process creates a phototoxic effect that targets cancer cells. Since PDT relies on light, it minimizes nonspecific targeting. To enhance the effectiveness of PDT, PSs are often loaded into nanocarriers, including ferritin.[29] However, dye sensitizers have concerns with biocompatibility and biodegradability. Encapsulating substances in ferritin nanocages frequently involves pH-mediated disintegration and reassembly, as well as denaturing buffer to disrupt protein structure. The pH-mediated approach is limited to compounds that are stable at low pH, around 2. As a result, ferritins have been engineered to disassemble at higher pH values ranging from 4 to 5.[17,30,31] Nonetheless, most encapsulation processes involve dialysis, which requires a large quantity of substrate input during encapsulation, resulting in substrate waste.[32] Finally, the integrity of the drugs encapsulated within ferritin must be evaluated throughout various temperatures and environmental conditions due to encapsulated chemical leakage.

To avoid the encapsulation process, we inserted the PDT function into ferritin by creating a nanoreactor (HFn-miniSOG) with HFn fused with the PS protein, miniSOG, at its *C*-terminus. MiniSOG is a flavin mononucleotide (FMN)-binding protein derived from the light-oxygen-voltage-sensing domain of *Arabidopsis thaliana* phototropin-2 that converts molecular oxygen into ROS, primarily $^1O_2$, when exposed to blue light.[33−35] In this study, soluble HFn-miniSOG was overexpressed in *E. coli* BL21(DE3) and self-assembled to form nanoparticles with an average hydrodynamic diameter of 22.4 ± 1.3 nm (Figure 1). As anticipated, HFn-miniSOG nanoparticles generated $^1O_2$ upon blue-light irradiation. Phototoxicity was evaluated in HepG2 and HeLa cells, which express different levels of TfR1. The viability of HepG2 cells was reduced by 63%, while HeLa cells showed a reduction of 34%. This difference in cell viability corresponds to the levels of TfR1 in each cell type. This study presents a straightforward method for producing ALL-IN-ONE protein nanoparticles for targeted photodynamic therapy (PDT) applications.

2. RESULTS AND DISCUSSION

2.1. Characterization of HFn-miniSOG. MiniSOG with a short encapsulation signal peptide was reported to be encapsulated in encapsulin nanoparticles.[36] Its cargo loading capacity was 7−9%, which represents ∼7 ± 2 miniSOG packaged per nanocompartment. To maximize the PDT impact, the number of miniSOG per nanocompartment should be carefully considered. As a result, we planned to overexpress a single recombinant fusion protein of ferritin and miniSOG in order to achieve maximum miniSOG incorporation. MiniSOG was fused with HFn at either its *N*- or *C*-terminus with a linker of 15 amino acids (G/S) for miniSOG-HFn and HFn-miniSOG, respectively. To facilitate purification, a His-tag was incorporated. These two recombinant fusion proteins were overexpressed individually in *E. coli* BL21(DE3). SDS-PAGE analysis revealed that miniSOG-HFn formed inclusion bodies while HFn-miniSOG was soluble (Figure S1). *E. coli* BL21(DE3) lysate containing HFn-miniSOG was subjected to Ni-NTA chromatography. The fractions that contained HFn-miniSOG were collected and filtered through a 0.22 μm filter to remove aggregated HFn-miniSOG nanoparticles. The resulting filtrate underwent biophysical characterization to analyze HFn-miniSOG. SDS-PAGE gel analysis confirmed successful purification, showing good purity (Figure S2a). The native-PAGE gel analysis revealed a high molecular weight band around 720 kDa, according to the native gel protein ladder (Figure S2b), indicating that HFn-miniSOG forms an 18-mer nanoparticle. To further confirm the morphology and size of the HFn-miniSOG nanoparticles, dynamic light scattering (DLS) measurements and transmission electron microscopy (TEM) imaging were performed (Figure 2c,d). In addition, HFn nanoparticles were prepared as a control. The DLS measurements of the HFn-miniSOG nanoparticles indicated a mean hydrodynamic diameter of 22.4 ± 1.3 nm (Figure 2c), compared to 15.7 ± 0.5 nm for the HFn nanoparticles (Figure 2a). The TEM image of negatively stained HFn-miniSOG showed filled particles (Figure 2d), while the HFn nanoparticles displayed a hollow structure (Figure 2b). These results suggest that the miniSOG may occupy the hollow structure of the HFn nanoparticles, leading to an increase in size.

Spectrophotometric analyses of absorbance and fluorescence were conducted to examine the impact of encapsulation on the properties of miniSOG. As illustrated in Figure 2f, both miniSOG and HFn-miniSOG exhibit nearly identical absorbance and fluorescence spectra, with an excitation wavelength (λ_{ex}) of 485 nm. The fluorescence spectra for both demonstrate emission maxima at 495 nm, accompanied by a shoulder at 525 nm. However, it was noted that the fluorescence intensity of HFn-miniSOG is reduced by 44.6% compared to that of miniSOG at the same concentration, as shown in Figure 2g. The FMN chromophore in miniSOG absorbs light energy, entering excited states to release energy as both fluorescence ($S_1 \rightarrow S_0$) or transfer energy to molecular oxygen via intersystem crossing ($S_1 \rightarrow T_1$) to generate $^1O_2$ predominantly via a type II mechanism.[33,34,37] Recently, new variants of miniSOG with improved photosensitization efficiencies were developed by eliminating intermolecular hydrogen bonds between FMN and the protein scaffold. This modification encourages the transfer of light energy toward triplet-state photosensitization, rather than singlet-state fluorescence. Consequently, the significant reduction in fluorescence observed in HFn-miniSOG during this study may be attributed to the structural rigidity in its FMN-binding region that occurs when forming the nanoparticle. As a result, HFn-miniSOG was expected to generate more $^1O_2$ compared to miniSOG.

2.2. Generation of $^1O_2$ from the Light-Activated HFn-miniSOG Nanoparticles. As shown in Figure 1, we hypothesized that the miniSOG in the HFn-miniSOG nanoparticles can convert molecular oxygen into $^1O_2$ when exposed to blue light. This highly reactive $^1O_2$ then diffuses into the surrounding area, where it can react with biomolecules. To test this hypothesis, we measured the ability of blue light-activated HFn-miniSOG to generate $^1O_2$ using the singlet oxygen sensor green (SOSG) reagent. SOSG selectively reacts with $^1O_2$ and does not react with hydroxyl radicals or superoxide, resulting in the emission of green fluorescence of

https://doi.org/10.1021/acsabm.5c00098
ACS Appl. Bio Mater. 2025, 8, 3909−3919

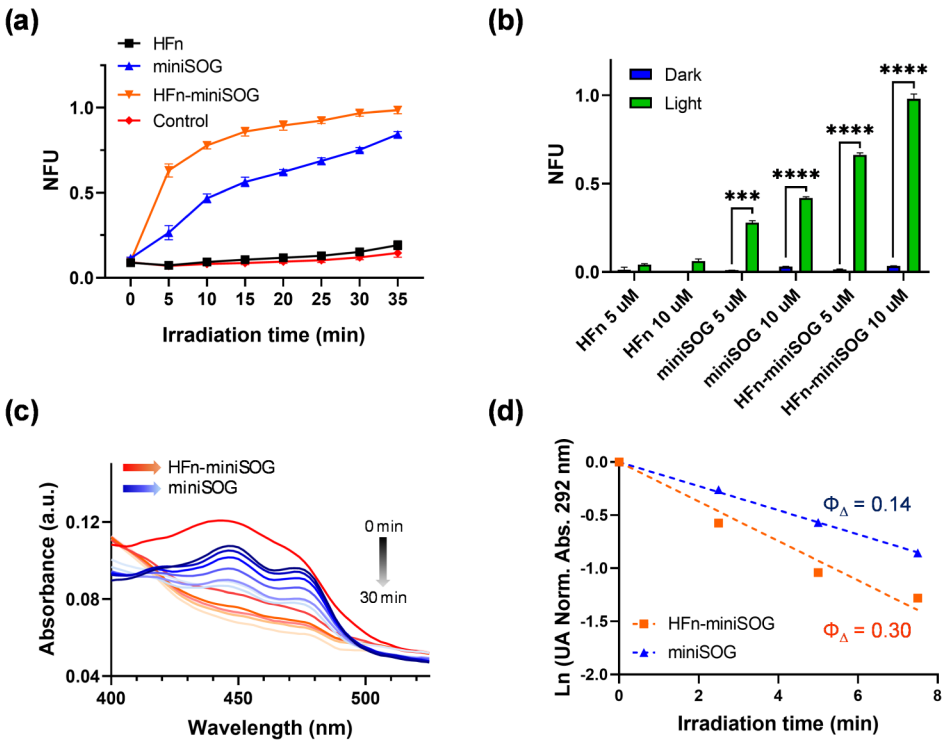

Figure 3. (a) $^1O_2$ generation by miniSOG and HFn-miniSOG with blue-light irradiation in the time course experiment of 35 min. HFn is the negative control. Control is SOSG alone. $^1O_2$ generation was monitored by measuring the fluorescence signal of SOSG endoperoxide (SOSG-EP), data presented as normalized fluorescence unit (NFU). Each fluorescence intensity was measured every 5 min and normalized to the highest fluorescence intensity value obtained in each data set. Error bars represent the mean ± standard deviation (n = 3). (b) NFU of SOSG-EP generated by 10 min light activation of HFn, miniSOG, and HFn-miniSOG at 5 and 10 μM, compared to dark conditions. (c) Absorbance spectra of miniSOG and HFn-miniSOG after blue-light irradiation were recorded every 5 min in the time course experiment of 30 min to know the integrity of FMN cofactor in miniSOG. The HFn-miniSOG absorbance at 450 nm decreased more rapidly than the miniSOG one. (d) Comparison of uric acid (UA) bleaching rate at 292 nm in the presence of miniSOG (blue) or HFn-miniSOG (orange) after irradiation.

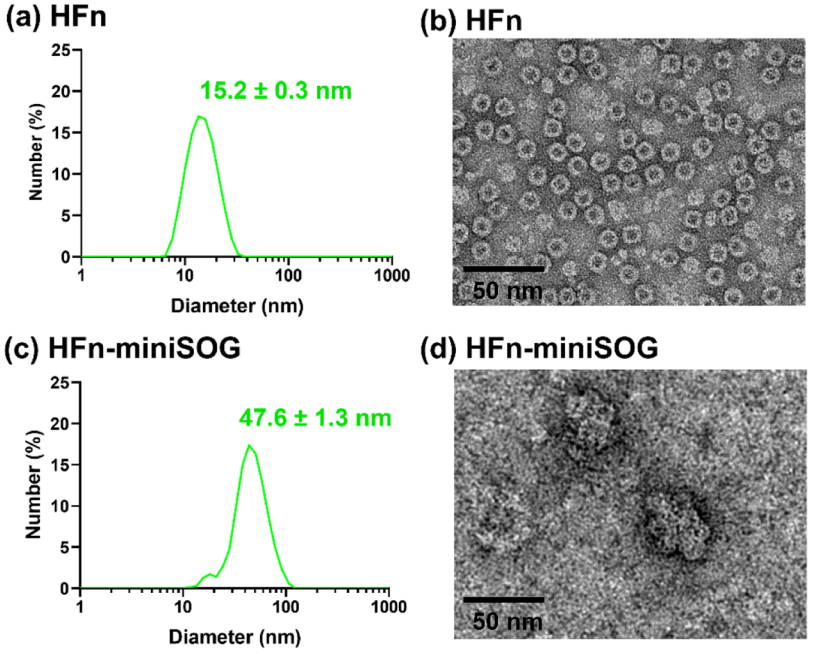

Figure 4. DLS analysis and TEM imaging of HFn (a,b) and HFn-miniSOG (c,d) after blue-light irradiation.

SOSG endoperoxide (SOSG-EP), with the excitation and emission maxima at 504 and 525 nm, respectively.[38] The fluorescence intensity corresponds to the amount of $^1O_2$ generated. Each sample of HFn, miniSOG, and HFn-miniSOG was mixed with SOSG in a 50 mM Tris buffer at pH 8. A control sample, consisting of SOSG in the same buffer, was also prepared. All samples were then irradiated with a blue LED at a wavelength of 450 nm for 35 min. The fluorescence

https://doi.org/10.1021/acsabm.5c00098
ACS Appl. Bio Mater. 2025, 8, 3909−3919

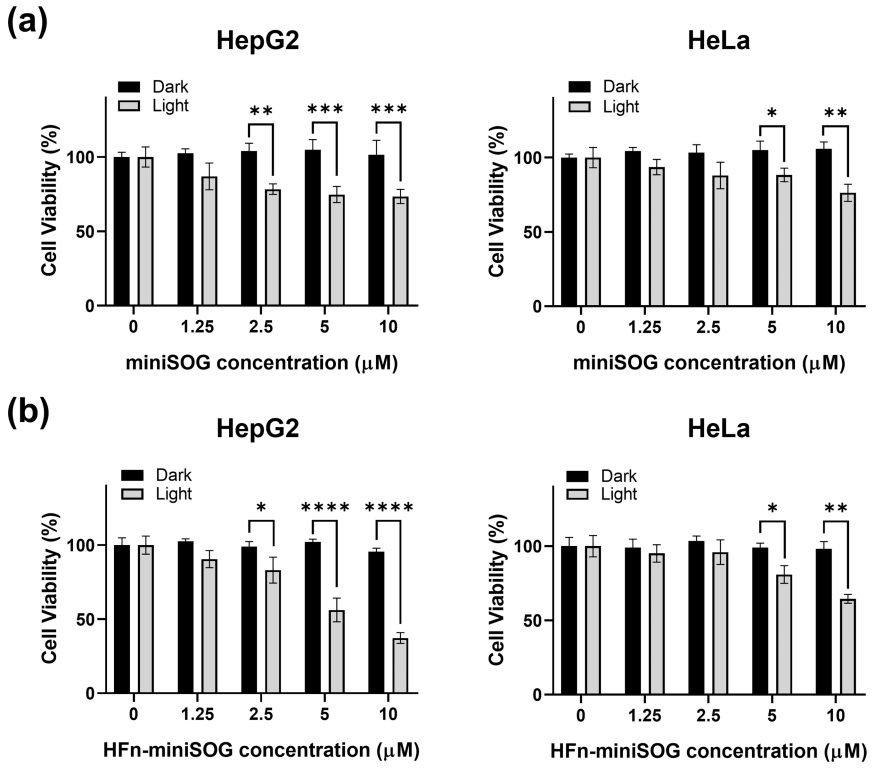

Figure 5. Cytotoxicity and phototoxicity of (a) miniSOG and (b) HFn-miniSOG. The cell viability of HepG2 cells (higher TfR1 expression) and HeLa cells (lower TfR1 expression) after incubation with various concentrations of miniSOG or HFn-miniSOG was determined by the MTT assay under dark and light conditions. The cells were irradiated with a blue light for 10 min. Values are expressed as means ± SD. Significance levels are indicated as follows: $*p \leq 0.05$, $**p \leq 0.01$, $***p \leq 0.001$, $****p \leq 0.0001$, using two-way ANOVA, with $n = 6$ from three independent experiments.

intensity was measured every 5 min (Figure 3a). SOSG displayed a minimal fluorescence intensity after light irradiation, as did the HFn sample, which lacks the ability to generate $^1O_2$. The fluorescence intensity of both HFn-miniSOG and miniSOG samples increased as a result of the formation of the SOSG-EP adduct,[38] especially HFn-miniSOG had higher fluorescence over time, suggesting more $^1O_2$ generation (Figures 3a,b and S3). It is possible that the rigidity of miniSOG in the protein nanoparticle increases the triplet state of FMN to molecular oxygen as compared to solely miniSOG. The fluorescence intensity of HFn-miniSOG and miniSOG (Figure 2g) supported this. Furthermore, the absorbance spectra of HFn-miniSOG and miniSOG following blue light irradiation have been studied to determine the stability of miniSOG's cofactor, FMN. In Figure 3c, the results showed that the flavin signal of HFn-miniSOG disappeared more rapidly compared to the one of miniSOG over 30 min. Both HFn-miniSOG and miniSOG's absorbance spectra showed that the FMN in HFn-miniSOG deteriorates more quickly than in miniSOG, with significant signal loss after 10 min as opposed to 30 min for miniSOG. This implies that HFn-miniSOG produces singlet oxygen more effectively in its initial stages, which speeds up cofactor decomposition and is important for its potential application in photodynamic therapy. Using the uric acid (UA) method (Scheme S1) to calculate the quantum yield (Φ_Δ) of $^1O_2$,[37,39] we found that HFn-miniSOG produced a higher Φ_Δ value than miniSOG (Figures 3d and S5, Table S1), confirming the photosensitization efficiency of HFn-miniSOG.

To further investigate the integrity of FMN, we measured the fluorescence spectra of HFn-miniSOG and miniSOG after blue light irradiation at 5 min intervals over a 30 min period (Figure S4). The results were consistent with the absorbance spectra; the intensities of both spectra showed a continuous decrease over time. Notably, the FMN spectrum of HFn-miniSOG nearly disappeared after just 10 min of irradiation (Figure S4b). These findings suggest that a significant amount of $^1O_2$ is generated during the initial phase, leading to the decomposition of the cofactor.[40]

Although ferritin nanoparticles have been described as robust nanostructures capable of withstanding severe pH and high temperatures, $^1O_2$ is very reactive with specific amino acids and can thus induce oxidative damage to protein structures. Therefore, we observed the structural change of HFn-miniSOG following irradiation by DLS analysis and TEM imaging compared to the control of HFn (Figure 4). Because HFn cannot produce $^1O_2$ under blue light irradiation (Figure 3a), there was no structural difference in DLS and TEM assessments before (Figure 2a,b) and after (Figure 4a,b) irradiation. The average diameter of the irradiated HFn-miniSOG was 47.6 ± 1.3 nm in DLS analysis (Figure 4c), which is about a 2-fold increase over the nonirradiated one (Figure 2c). The nanoparticle shape was subsequently studied by TEM imaging, which revealed nanoparticle aggregation (Figure 4d). The HFn-miniSOG's structural integrity and stability loss can be attributable to $^1O_2$ produced by the irradiated miniSOG, which can severely destroy its surrounding protein shell. This is consistent with ferritin nanoparticles encapsulating the potent PS, ZnF16Pc, which were then destroyed by $^1O_2$ produced by the light-activated ZnF16Pc molecule.[29]

https://doi.org/10.1021/acsabm.5c00098
ACS Appl. Bio Mater. 2025, 8, 3909−3919

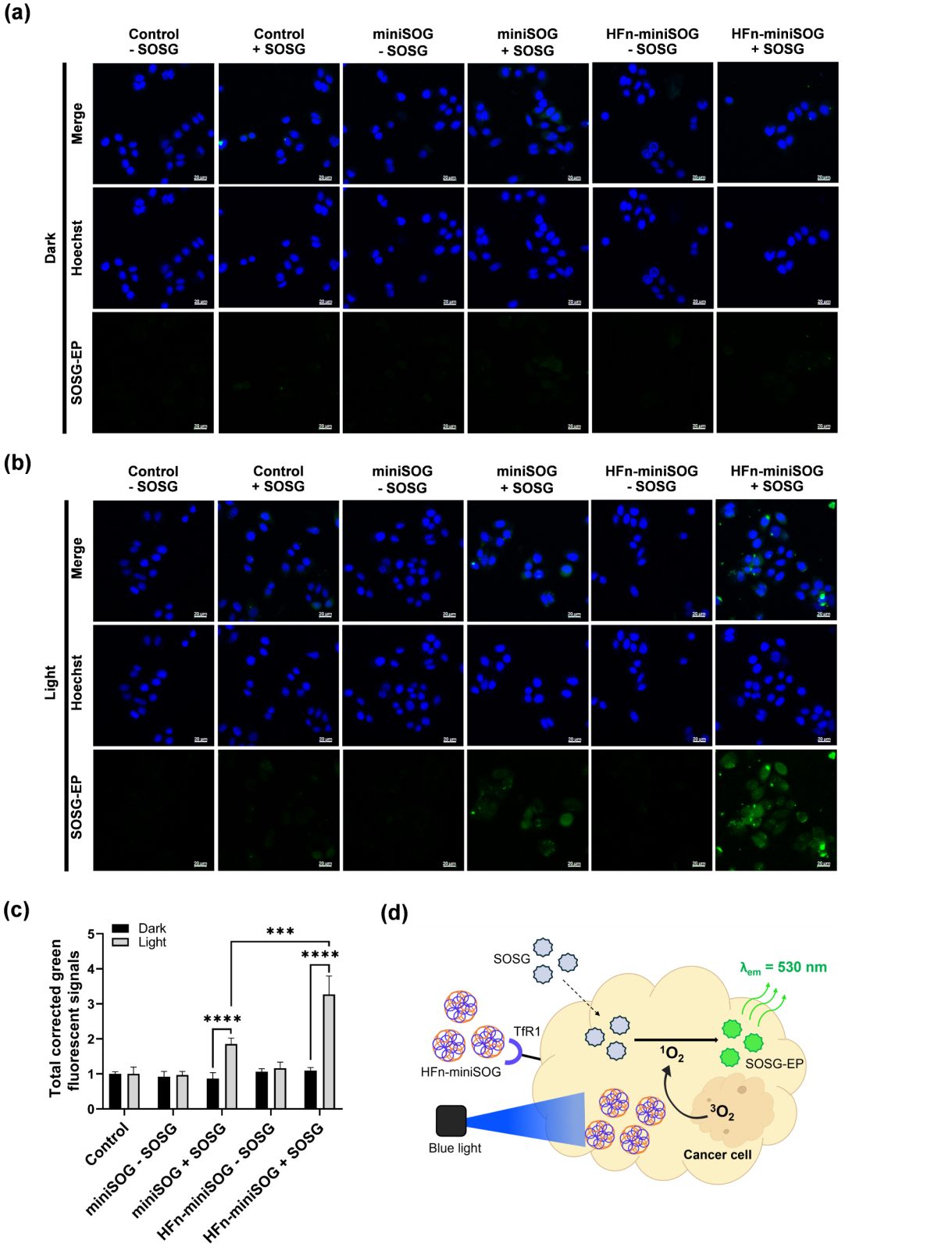

Figure 6. Intracellular $^1O_2$ generation by HFn-miniSOG in HepG2 cells. Confocal microscopy images of HepG2 cells treated with miniSOG or HFn-miniSOG-treated cells in the absence (a) or presence (b) of blue-light irradiation. Scale bar: 20 μm. (c) The corrected green fluorescent signals represent $^1O_2$ generation levels inside HepG2 cells for different experiments in (b). Values represent means ± SD (*$p \leq 0.05$, **$p \leq 0.01$, ***$p \leq 0.001$, ****$p \leq 0.0001$), two-way ANOVA, $n = 3$ from three independent experiments. (d) Schematic illustrates the generation of intracellular singlet oxygen ($^1O_2$). The photooxidation of SOSG inside HepG2 cells produces SOSG-EP, leading to a green fluorescent signal.

2.3. *In Vitro* PDT Applications of HFn-miniSOG Nanoparticles. PDT utilizes light-induced PSs that convert intracellular molecular oxygen into reactive oxygen species (ROS). This process damages cellular components and

https://doi.org/10.1021/acsabm.5c00098
ACS Appl. Bio Mater. 2025, 8, 3909−3919

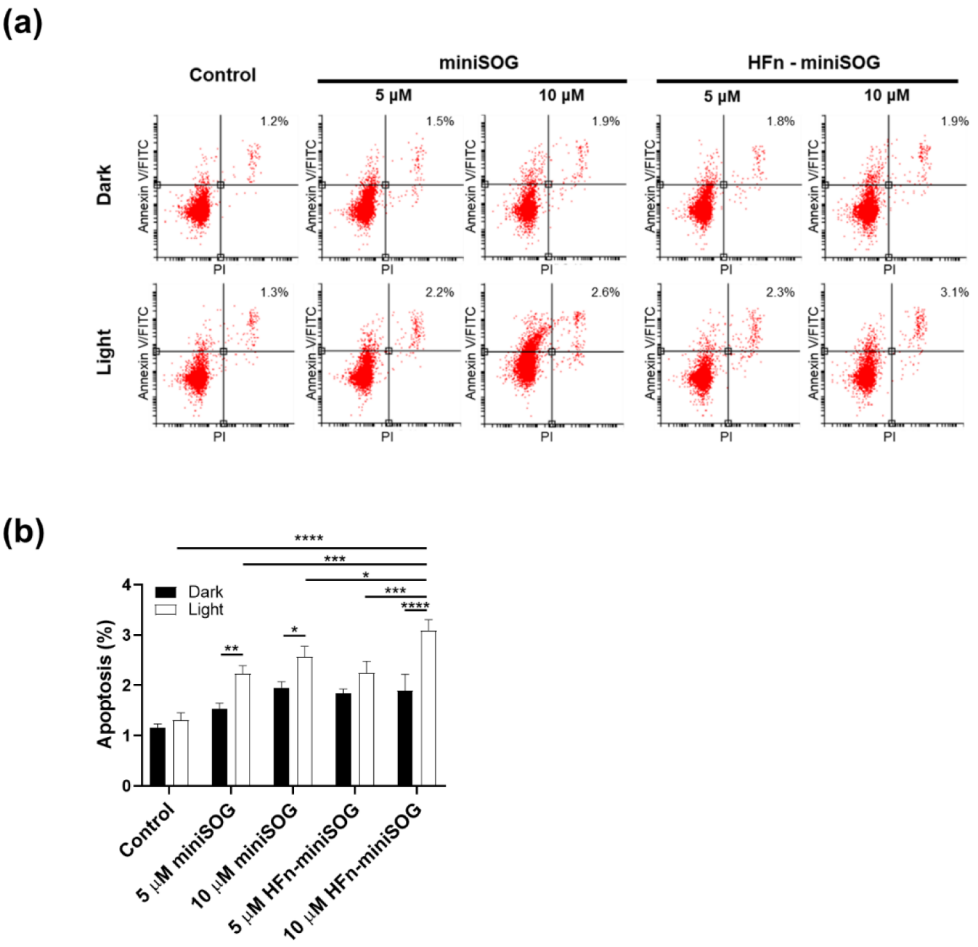

Figure 7. Cell death caused apoptosis induced by PDT of HFn-miniSOG. (a) Cytometry analysis: effect of different doses of miniSOG and HFn-miniSOG under blue-light irradiation on apoptosis in HepG2 cells compared to nonirradiated ones. (b) Histogram analysis of cytometry results. Values represent means ± SD (*$p \leq 0.05$, **$p \leq 0.01$, ****$p \leq 0.0001$), two-way ANOVA, $n = 3$ from three independent experiments.

ultimately leads to cell death. MiniSOG, which contains the FMN cofactor, can generate $^1O_2$ when exposed to blue light, making it a potentially valuable tool for PDT. However, miniSOG has not progressed to preclinical studies due to limitations in dosage and localization, which reduce its therapeutic efficacy. Ferritin is versatile and can target tumor cells that have high levels of TfR1 on their membranes. To explore this concept, HFn-miniSOG was used to assess its feasibility and compare its performance in downstream *in vitro* experiments with that of miniSOG.

To test whether miniSOG or HFn-miniSOG has a cytotoxicity effect on tumor cells, this study used cell lines with different TfR1 expression levels, HepG2 (higher TfR1 expression) and HeLa (lower TfR1 expression) cells, as models. HepG2 has 2.5-fold higher TfR1 expression than HeLa cells.[41] The cells were treated with miniSOG or HFn-miniSOG with increasing concentrations (0, 1.25, 2.5, 5, and 10 μM) for 6 h before assessing cell viability using MTT assay. In the absence of light activation, neither miniSOG nor HFn-miniSOG exhibited significant cytotoxicity compared to untreated cells (Figure 5). However, when cells were treated under the same conditions and subsequently exposed to blue light for 10 min, a phototoxic effect was observed. This effect was noted with both miniSOG (Figure 5a) and HFn-miniSOG (Figure 5b) in a dosage-dependent manner. As expected, the viability of HepG2 cells preincubated with 10 μM HFn-miniSOG under light irradiation was significantly reduced by approximately 63% due to the higher expression of TfR1 compared to HeLa cells, which had a 34% reduction in cell viability.[41]

The generation of intracellular $^1O_2$ by HFn-miniSOG in HepG2 cells was further confirmed using SOSG, a probe that detects $^1O_2$ produced by internalized nanoparticles. SOSG emits a green fluorescence signal upon reaction with $^1O_2$, which can be observed through confocal microscopy. As illustrated in Figure 6a, HepG2 cells treated with 10 μM of either miniSOG or HFn-miniSOG did not exhibit any fluorescence signal in the dark, similar to the untreated control. In contrast, cells treated with 10 μM of miniSOG or HFn-miniSOG, followed by blue light irradiation, showed significant green fluorescence (Figure 6b). Notably, HFn-miniSOG-treated cells displayed a 1.4-fold increase in fluorescence signals compared to those treated with miniSOG (Figure 6c). These results align with the findings in Figure 5b, indicating that HFn-miniSOG generates more ROS, which contributes to cell death. Additionally, the schematic in Figure 6d illustrates the detection of SOSG-EP generated from singlet oxygen production following photosensitizer activation.

To assess whether intracellular $^1O_2$ induces apoptosis in cancer cells, we conducted annexin V/PI staining followed by flow cytometry analysis to examine photodynamic-assisted apoptosis. As shown in Figure 7, light irradiation increased the

https://doi.org/10.1021/acsabm.5c00098
ACS Appl. Bio Mater. 2025, 8, 3909−3919

apoptotic rate in cells treated with different concentrations of miniSOG or HFn-miniSOG compared to the untreated cells. The treatment of 10 μM HFn-miniSOG resulted in the highest apoptotic rate at approximately 3.1%. However, the relatively low percentage of apoptotic cells suggests that apoptosis may not be the predominant mechanism of cell death induced by this nanoparticle. This implies that other forms of cell death, such as necrosis or autophagy, may also play a role. For instance, studies have demonstrated that miniSOG can induce necrosis through oxidative stress,[42] lysosomal membrane permeabilization,[43] and autophagic processes.[44] Therefore, these *in vitro* investigations demonstrate that photosensitizing HFn-miniSOG is transported into tumor cells and activated by light to produce cytotoxic $^1O_2$, which decreases cell viability and promotes apoptotic cell death.

3. CONCLUSION

HFn was selected as a scaffold for targeted drug delivery due to its ability to produce stable nanoparticles that are resistant to heat and can withstand low and high pH levels. Additionally, it can specifically target cancer cells that overexpress TfR1, which is the receptor for HFn. Rather than encapsulating a drug within HFn nanoparticles, which is the typical approach, we fused HFn with miniSOG to create the HFn-miniSOG protein. We found that HFn-miniSOG can self-assemble into nanoparticles with an average size of 22.4 ± 1.3 nm and produces $^1O_2$ when exposed to blue light. Additionally, HFn-miniSOG is capable of generating more singlet oxygen ($^1O_2$) compared to miniSOG alone over the same period. This suggests that the encapsulation of miniSOG enhances the energy transfer from flavin mononucleotide (FMN) to molecular oxygen in the triplet state. The generated $^1O_2$ also leads to the decomposition of the flavin cofactor and the aggregation of HFn-miniSOG nanoparticles.

We further assessed the phototoxicity of HFn-miniSOG in HepG2 cells, which express higher levels of TfR1 compared to HeLa cells, to showcase its specific capabilities for PDT. Following light exposure, the viability of HepG2 cells decreased by 63%, while HeLa cells experienced a 34% reduction. Notably, HFn-miniSOG did not show significant cytotoxicity in the absence of light.

This study introduces a straightforward method for producing all-in-one protein nanoparticles tailored for targeted PDT applications. The goal is to enhance the effectiveness of cancer treatment while minimizing side effects on healthy cells. However, it is worth noting that HFn-miniSOG is activated by short-wavelength blue light, which has limited tissue penetration and may restrict its *in vivo* applications. To overcome this limitation, interventional fiber optic therapy could be utilized to deliver light to specific tissue areas through surgical procedures or endoscopy.[45,46]

4. EXPERIMENTAL SECTION

4.1. Materials. Chemicals and reagents used in this study were purchased from Acros, Carlo Erba, Cytiva, Himedia, Thermo Scientific, TCI, Merck, Supelco, and Sigma-Aldrich. The power density of the blue light (450 nm) is 140 mW/cm^2 for every experiment.

4.2. HFn Overexpression and Purification. Ten milliliters of an overnight culture of *E. coli* BL21(DE3) containing pET-HFn were inoculated into 1 L Luria−Bertani (LB) medium with the final concentration of 100 μg/mL ampicillin. The culture was incubated at 37 °C with the shaking speed of 200 rpm. The protein overexpression was induced by the addition of isopropyl-β-D-1-thiogalactopyranoside (IPTG) with the final concentration of 0.5 mM when the culture's OD600 reached about 0.6 to 0.7. After that, the culture was incubated at the same conditions for another 4−6 h. Finally, the cells were harvested by centrifugation at 5,000 rpm at 8 °C for 20 min.

For protein purification, cell pellets were resuspended in lysis buffer (300 mM NaCl, 50 mM Tris, pH 8) containing 1 mM PMSF and then sonicated in ice bath for 30 s (1.5 s cycle, 50% duty) three time. Cellular debris was removed by centrifugation at 12,000 rpm at 8 °C for 40 min. The resultant supernatant was heated at 70 °C for 20 min, then chilled on ice. The solution was centrifuged at 12,000 rpm at 8 °C for 40 min. The obtained supernatant was filtered through a 0.22 μm filter to remove any precipitate followed by buffer exchange to 50 mM Tris (pH 8.0) using an Amicon Ultra-15 centrifugal filter unit (10-kDa cutoff). Finally, the protein was purified by HiTrap DEAE FF column (Cytiva) using ÄKTA Start ion-exchange chromatography (Cytiva). The HFn protein was eluted using an increasing gradient of NaCl concentration. Lastly, the purified HFn protein was desalted in 100 mM Tris (pH 7.5) containing 20% glycerol by Amicon Ultra-15 centrifugal filter unit (10-kDa cutoff). The protein was aliquoted and stored at −20 °C.

4.3. MiniSOG Overexpression and Purification. Ten milliliters of an overnight culture of *E. coli* BL21(DE3) containing pET30a-miniSOG was inoculated into 1 L LB medium containing the final concentration of 50 μg/mL kanamycin. The culture was incubated at 37 °C with the shaking speed of 200 rpm. The protein overexpression was induced by the addition of IPTG with the final concentration of 200 μM when the culture's OD_{600} reached about 0.6−0.7. After that, the culture was incubated at the same conditions for another 4−6 h. Finally, the cells were harvested by centrifugation at 5,000 rpm at 8 °C for 20 min.

For protein purification, cell pellets were resuspended in lysis buffer (300 mM NaCl, 50 mM Na_2HPO_4, 10 mM imidazole, pH 8) containing 1 mM PMSF, and then sonicated in ice bath for 30 s (1.5 s cycle, 50% duty) for three times. Cellular debris was removed by centrifugation at 12,000 rpm at 8 °C for 40 min. The resultant supernatant was filtered through a 0.45 μm filter and then loaded into a Ni-NTA column (QIAGEN). The protein was eluted by following the manufacturer's instructions. The fractions containing miniSOG identified by SDS-PAGE analysis were pooled and concentrated by an Amicon Ultra-15 centrifugal filter unit (10-kDa cutoff). After that, the concentrated miniSOG solution was incubated with FMN at a 1:2 molar ratio of miniSOG and FMN in the dark for 30 min. Finally, the protein was desalted using a 10-DG column (BioRad) pre-equilibrated with the desalting buffer (100 mM Tris-HCl buffer, 20% glycerol, pH 7.5). The miniSOG concentration was determined using the extinction coefficient of flavin (ε = 12,500 $M^{-1}\cdot cm^{-1}$ at 450 nm). The purified protein was aliquoted and stored at −20 °C.

4.4. HFn-miniSOG Overexpression and Purification. 10 mL of an overnight culture of *E. coli* BL21(DE3) containing pET30a-HFn-miniSOG was inoculated into 1 L Terrific Broth (TB) medium with the final concentration of 50 μg/mL kanamycin. The culture was incubated at 37 °C with the shaking speed of 200 rpm. When the culture's OD_{600} reached about 0.6 to 0.7, the protein overexpression was induced by the addition of IPTG with the final concentration of 500 μM. After that, the culture was incubated at the same condition for another 4−6 h. The cells were harvested by centrifugation at 5,000 rpm at 8 °C for 20 min. Cell pellets were resuspended in lysis buffer (300 mM NaCl, 50 mM Na_2HPO_4, 10 mM imidazole, pH 8) containing 1 mM PMSF and then sonicated in ice bath for 30 s (1.5 s cycle, 50% duty) three times. Cellular debris was removed by centrifugation at 12,000 rpm at 8 °C for 40 min. The resultant supernatant was filtered through a 0.45 μm filter and then loaded into a Ni-NTA column (QIAGEN). The protein was eluted by following the manufacturer's instructions. The fractions containing HFn-miniSOG identified by SDS-PAGE analysis were pooled and concentrated by using an Amicon Ultra-15 centrifugal filter unit (10-kDa cutoff). After that, the concentrated HFn-miniSOG solution was incubated with FMN at a 1:2 molar ratio of HFn-miniSOG and FMN in the dark for 30 min. Finally, the protein was desalted using a 10-DG column (BioRad) pre-equilibrated with the desalting buffer

https://doi.org/10.1021/acsabm.5c00098
ACS Appl. Bio Mater. 2025, 8, 3909−3919

(100 mM Tris-HCl buffer, 20% glycerol, pH 7.5) followed by filtration using a 0.22 μm filter. The HFn-miniSOG concentration of HFn-miniSOG was determined using the extinction coefficient of flavin (ε = 12,500 $M^{-1}\cdot cm^{-1}$ at 450 nm). The purified protein was aliquoted and stored at −20 °C.

4.5. Absorbance Spectroscopy of miniSOG and HFn-miniSOG. The absorbance spectra of 10 μM miniSOG, or HFn-miniSOG in a final volume of 200 μL 50 mM Tris (pH 8) were measured by the CLARIOstar Plus plate reader (BMG LABTECH, Germany).

4.6. Fluorescence Spectroscopy of miniSOG and HFn-miniSOG. The fluorescence emission intensity ($\lambda_{ex}/\lambda_{em}$ = 485/520 nm) of 10 μM HFn, miniSOG or HFn-miniSOG in a final volume of 2 mL 50 mM Tris (pH 8) was measured using Duetta fluorescence spectrometer (HORIBA Scientific) using a quartz cuvette with 1 cm path length.

4.7. Dynamic Light Scattering (DLS) Analyses. Purified protein samples were diluted to final concentrations of 0.5 mg/mL in PBS buffer, filtered through Minisart syringe filters, poly(ether sulfone), pore size 0.22 μm, nonsterile (Sartorius Inc.), and analyzed with the DynaPro NanoStar (Wyatt Technology Ltd.) at 25 °C in 1 mL disposable polystyrene cuvettes. Measurements were performed in triplicates. Size distributions derived from intensity distributions were presented.

4.8. Field Emission Gun Transmission Electron Microscope (FEG-TEM) Analyses. Purified HFn or HFn-miniSOG protein samples were diluted to final concentrations of 50−75 μg/mL in PBS buffer. The HFn or HFn-miniSOG proteins, after blue light treatment for 10 min, were prepared with a concentration of 100 μg/mL. Glow discharge of the Formvar/Carbon Supported Copper Grids, size 400 mesh (Sigma-Aldrich), was performed with Emitech K100X (Quorum Technologies Ltd.) at 25 mA for 30 s. Five μL of each sample were deposited onto the glow-discharged grids and incubated for 90 s. Excess solution was then wicked away with filter papers. Grids were then rinsed thrice with 5 μL of ddH2O, with the solution wicked away immediately. Grids were stained with 5 μL of aqueous, freshly filtered 1% uranyl acetate for 1 min, with the solution then wicked away, and air-dried in a desiccator. Images were collected with the FEI Tecnai G2F20 Super TWIN FEG-TEM at an accelerating voltage of 120 kV.

4.9. $^1O_2$ Detection. $^1O_2$ generation was measured in each protein solution containing the fluorescent probe SOSG according to the manufacturer's protocol (Invitrogen, USA). Each sample solution contained 10 μM SOSG and 10 μM HFn, HFn-miniSOG, or miniSOG in 200 μL of 50 mM Tris (pH 8). Every mixture was irradiated by blue light for different time periods. At each time point, the fluorescence signal from SOSG-EP ($\lambda_{ex}/\lambda_{em}$ = 504/525 nm) in every sample was measured CLARIOstar Plus plate reader (BMG LABTECH, Germany).

4.10. $^1O_2$ Quantum Yield Measurements. Indirect measurement of $^1O_2$ was performed using uric acid (UA) as a chemical probe. The absorption spectra of a sample solution containing 50 μM UA and 2.5 μM FMN, miniSOG, or HFn-miniSOG in a total volume of 2 mL were measured on a UV−vis spectrophotometer (Shimadzu/UV-1900i). The absorbances of UA at 292 and 315 nm were measured every 2.5 min of the irradiation time course experiment of 20 min. Upon the reaction with $^1O_2$, UA forms a hydroperoxide intermediate resulting the decreasing of absorbance at 292 nm. Consequently, the absorbance at 292 nm decreases following biexponential kinetics. Since the breakdown of the hydroperoxide intermediate does not rely on oxygen, the initial decay rate (k_1) solely represents the interaction with $^1O_2$. Additionally, this reaction can be observed at 315 nm, where the formation of the intermediate (k_1) is indicated by an increase in absorbance. The singlet oxygen quantum yield (Φ_Δ^{sample}) was calculated using FMN in UA as a reference (Φ_Δ^{ref} = 0.32).

$$\gamma_\Delta \propto \frac{k_1}{N_{Abs}} \tag{1}$$

$$\Phi_\Delta^{sample} = \frac{\Phi_\Delta^{ref}}{\gamma_\Delta^{ref}}\gamma_\Delta^{sample} \tag{2}$$

4.11. *In Vitro* Cytotoxicity and Phototoxicity. HeLa and HepG2 cells were cultured in Dulbecco's modified Eagle's medium (DMEM) supplemented with 10% FBS and 1% penicillin-streptomycin at 37 °C in a 5% CO_2-containing humidified incubator. For *in vitro* cytotoxicity and phototoxicity studies, HeLa or HepG2 cells were seeded into a 96-well microplate with about 5.0 × 10^3 cells per well, followed by incubation at 37 °C for 24 h. First, the effect of laser irradiation on cell viability was investigated by exposing cells to a 450 nm blue laser for 10 min. To evaluate the cytotoxicity of every protein, cells were incubated with different concentrations (0, 1.25, 2.5, 5.0, and 10.0 μM) of miniSOG or HFn-miniSOG at 37 °C in the dark for 6 and 24 h. To evaluate phototoxicity, every cell culture in the cytotoxicity experiments was irradiated by a blue lamp for 10 min.

To quantify cell viability, the cells in each well were washed once with PBS to remove noninternalized protein, and then fresh growth medium was added. The cells were cultivated for another 24 h, and cell viability was finally determined by using the 3-(4,5-dimethylthiazol-2-yl)-2,5-diphenyltetrazolium bromide (MTT) cell viability assay (Invitrogen, USA) according to the manufacturer's protocol.

4.12. Intracellular $^1O_2$ Generation Detection. To visualize intracellular $^1O_2$ generation *in vitro*, HepG2 cells were seeded on 2 sets of eight-well chambered cover glass (Nunc Lab-Tek II Chamber Slide) and incubated at 37 °C under 5% CO_2 for 24 h. After that, the cultured mediums were replaced with fresh growth mediums containing 10 μM HFn-miniSOG or miniSOG followed by another 6 h incubation. Then, the cells were washed with PBS three times, followed by adding 20 μM SOSG for 2 h incubation. Then the cells were washed with PBS three times, followed by adding fresh culture medium. Finally, each sample was irradiated by a blue light lamp for 10 min. The nonirradiated set was used as a control.

After irradiation, the cells were incubated at 37 °C under 5% CO_2 for 20 min. Then the medium was replaced with the medium containing 1.0 μM Hoechst 33342 (Thermo Fisher Scientific), followed by incubation in the dark until performing fluorescence observation. Laser scanning confocal microscopy (LSCM) with a 60× oil immersion objective lens (Nikon A1Rsi) was used to observe fluorescence products. Hoechst 33342 was excited at 405 nm, while SOSG was detected using a 488 nm excitation laser.

4.13. Apoptosis Detection by Flow Cytometry. HepG2 cells were seeded into six-well cell culture plates with about 5 × 10^5 cells/well and incubated at 37 °C under 5% CO_2 for 24 h. After that, the medium was removed, and the solution containing HFn-miniSOG or miniSOG in DMEM was added to make the final concentrations of 5 and 10 μM. After incubation for 6 h, the culture medium was replaced with DMEM, followed by overnight incubation. After that, the cells were harvested and washed with cold PBS three times. Then, the cells were resuspended in 0.5 mL of 1× Annexin binding buffer (Thermo Fisher Scientific from Tali Apoptosis Kit), followed by adding 25 μL of Annexin V fluorescein conjugate (Annexin V Alexa Fluor TM 488, Thermo Fisher Scientific). After the solution was incubated at room temperature for 15 min, 0.5 μL of 1 mg/mL Propidium iodide (PI, Thermo Fisher Scientific) was added. Finally, the cells were analyzed by flow cytometry using an Attune NxT Flow Cytometer (Thermo Fisher Scientific).

4.14. Statistical Analysis. Statistical analyses were performed using GraphPad Prism 8.0 (GraphPad Software, Inc.). The results (presented as the mean ± SD) were calculated from three independent experiments. The one-way and two-way ANOVAs, followed by Tukey's correction, were used to compare multiple data sets. ImageJ was used to quantify corrected total cell fluorescence data, which was represented as mean ± SD. $p < 0.05$ was considered significant.

https://doi.org/10.1021/acsabm.5c00098
ACS Appl. Bio Mater. 2025, 8, 3909−3919

■ ASSOCIATED CONTENT

Supporting Information

The Supporting Information is available free of charge at https://pubs.acs.org/doi/10.1021/acsabm.5c00098.

Protein sequence information; SDS-PAGE and native gel analysis; fluorescence analysis of SOSG, miniSOG, and HFn-miniSOG before and after irradiation; photosensitized oxygenation of UA with hydroperoxide intermediates upon reaction with $^1O_2$; determination of $^1O_2$ quantum yield using uric acid (UA) as a probe; values of Φ_Δ obtained with the calculation of k_1 from UA bleaching in PBS (PDF)

■ AUTHOR INFORMATION

Corresponding Authors

Rung-Yi Lai − *School of Chemistry, Institute of Science, Suranaree University of Technology, Nakhon Ratchasima 30000, Thailand;* orcid.org/0000-0002-2076-0969; Email: rylai@sut.ac.th

Yane-Shih Wang − *Institute of Biological Chemistry, Academia Sinica, Taipei 11529, Taiwan; Institute of Biochemical Sciences, National Taiwan University, Taipei 10617, Taiwan;* orcid.org/0000-0003-2356-9577; Email: yaneshihwang@gate.sinica.edu.tw, ericyswang@gmail.com

Authors

Narathip Naradun − *School of Chemistry, Institute of Science, Suranaree University of Technology, Nakhon Ratchasima 30000, Thailand*

Piyasiri Chueakwon − *School of Chemistry, Institute of Science, Suranaree University of Technology, Nakhon Ratchasima 30000, Thailand*

Anyanee Kamkaew − *School of Chemistry, Institute of Science, Suranaree University of Technology, Nakhon Ratchasima 30000, Thailand;* orcid.org/0000-0003-1203-2686

Kai-Yu Hsu − *Institute of Biological Chemistry, Academia Sinica, Taipei 11529, Taiwan*

Man Nee Lee − *Institute of Biological Chemistry, Academia Sinica, Taipei 11529, Taiwan*

Kantapat Chansaenpak − *National Nanotechnology Center, National Science and Technology Development Agency, Pathum Thani 12120, Thailand;* orcid.org/0000-0002-5462-9897

Complete contact information is available at: https://pubs.acs.org/10.1021/acsabm.5c00098

Author Contributions

[⊥]N.N. and P.C. contributed equally to this work.

Notes

The authors declare no competing financial interest.

■ ACKNOWLEDGMENTS

This project is funded by the National Research Council of Thailand (NRCT) and Suranaree University of Technology (SUT) under grant number N42A650326. This work was supported by (i) Suranaree University of Technology (SUT), (ii) Thailand Science Research and Innovation (TSRI), and (iii) the National Science, Research and Innovation Fund (NSRF) (Project code: 204253). N.N. is supported by the Development and Promotion of Science and Technology Talents Project (DPST) Scholarship for his PhD study. Dr. Y.-S.W. is supported by Academia Sinica (AS) and the National Science and Technology Council (NSTC 113-2113-M-001-006 and NSTC 112-2113-M-001-015), Taiwan. Dr. Y.-S.W. acknowledges DynaPro NanoStar data collected at the AS Biophysics Core Facility (AS-CFII-111-201) and TEM at the AS Biological Electron Microscopy Core Facility.

■ REFERENCES

(1) Liu, C.; Yang, M.; Zhang, D.; Chen, M.; Zhu, D. Clinical Cancer Immunotherapy: Current Progress and Prospects. *Front. Immunol.* **2022**, *13*, 961805.

(2) Davis, M. E.; Chen, Z.; Shin, D. M. Nanoparticle Therapeutics: An Emerging Treatment Modality for Cancer. *Nat. Rev. Drug Discovery* **2008**, *7* (9), 771−782.

(3) Wang, S.; Cheng, K.; Chen, K.; Xu, C.; Ma, P.; Dang, G.; Yang, Y.; Lei, Q.; Huang, H.; Yu, Y.; Fang, Y.; Tang, Q.; Jiang, N.; Miao, H.; Liu, F.; Zhao, X.; Li, N. Nanoparticle-Based Medicines in Clinical Cancer Therapy. *Nano Today* **2022**, *45*, 101512.

(4) Bajpai, S.; Tiwary, S. K.; Sonker, M.; Joshi, A.; Gupta, V.; Kumar, Y.; Shreyash, N.; Biswas, S. Recent Advances in Nanoparticle-Based Cancer Treatment: A Review. *ACS Appl. Nano Mater.* **2021**, *4* (7), 6441−6470.

(5) Liu, S.; Yan, Z.; Huang, Z.; Yang, H.; Li, J. Smart Nanocarriers for the Treatment of Retinal Diseases. *ACS Appl. Bio Mater.* **2024**, *7* (4), 2070−2085.

(6) Li, J.-X.; Shu, N.; Zhang, Y.-J.; Tong, Q.-S.; Wang, L.; Zhang, J.-Y.; Du, J.-Z. Self-Assembled Nanoparticles from the Amphiphilic Prodrug of Resiquimod for Improved Cancer Immunotherapy. *ACS Appl. Mater. Interfaces* **2024**, *16* (20), 25665−25675.

(7) Delfi, M.; Sartorius, R.; Ashrafizadeh, M.; Sharifi, E.; Zhang, Y.; De Berardinis, P.; Zarrabi, A.; Varma, R. S.; Tay, F. R.; Smith, B. R.; Makvandi, P. Self-Assembled Peptide and Protein Nanostructures for Anti-Cancer Therapy: Targeted Delivery, Stimuli-Responsive Devices and Immunotherapy. *Nano Today* **2021**, *38*, 101119.

(8) Kianfar, E. Protein Nanoparticles in Drug Delivery: Animal Protein, Plant Proteins and Protein Cages, Albumin Nanoparticles. *J. Nanobiotechnol.* **2021**, *19* (1), 159.

(9) Lee, S.; Pham, T. C.; Bae, C.; Choi, Y.; Kim, Y. K.; Yoon, J. Nano Theranostics Platforms That Utilize Proteins. *Coord. Chem. Rev.* **2020**, *412*, 213258.

(10) Yang, M.; Kim, Y.; Youn, S.-Y.; Jeong, H.; Shirbhate, M. E.; Uhm, C.; Kim, G.; Nam, K. T.; Cha, S.-S.; Kim, K. M.; Yoon, J. Conversion of Albumin into a BODIPY-like Photosensitizer by a Flick Reaction, Tumor Accumulation and Photodynamic Therapy. *Biomaterials* **2025**, *313*, 122792.

(11) Tiryaki, E.; Álvarez-Leirós, C.; Majcherkiewicz, J. N.; Chariou, P. L.; Maceira-Campos, M.; Bodelón, G.; Steinmetz, N. F.; Salgueiriño, V. Magnetically Induced Thermal Effects on Tobacco Mosaic Virus-Based Nanocomposites for a Programmed Disassembly of Protein Cages. *ACS Appl. Bio Mater.* **2024**, *7* (7), 4804−4814.

(12) Demchuk, A. M.; Patel, T. R. The Biomedical and Bioengineering Potential of Protein Nanocompartments. *Biotechnol. Adv.* **2020**, *41*, 107547.

(13) Mohanty, A.; Parida, A.; Raut, R. K.; Behera, R. K. Ferritin: A Promising Nanoreactor and Nanocarrier for Bionanotechnology. *ACS Bio Med. Chem. Au* **2022**, *2* (3), 258−281.

(14) Jin, Y.; He, J.; Fan, K.; Yan, X. Ferritin Variants: Inspirations for Rationally Designing Protein Nanocarriers. *Nanoscale* **2019**, *11* (26), 12449−12459.

(15) Song, N.; Zhang, J.; Zhai, J.; Hong, J.; Yuan, C.; Liang, M. Ferritin: A Multifunctional Nanoplatform for Biological Detection, Imaging Diagnosis, and Drug Delivery. *Acc. Chem. Res.* **2021**, *54* (17), 3313−3325.

(16) Chen, H.; Tan, X.; Han, X.; Ma, L.; Dai, H.; Fu, Y.; Zhang, Y. Ferritin Nanocage Based Delivery Vehicles: From Single-, Co- to Compartmentalized- Encapsulation of Bioactive or Nutraceutical Compounds. *Biotechnol. Adv.* **2022**, *61*, 108037.

(17) Ahn, B.; Lee, S.-G.; Yoon, H. R.; Lee, J. M.; Oh, H. J.; Kim, H. M.; Jung, Y. Four-Fold Channel-Nicked Human Ferritin Nanocages for Active Drug Loading and PH-Responsive Drug Release. *Angew. Chem., Int. Ed.* **2018**, *57* (11), 2909−2913.
(18) Inoue, I.; Chiba, M.; Ito, K.; Okamatsu, Y.; Suga, Y.; Kitahara, Y.; Nakahara, Y.; Endo, Y.; Takahashi, K.; Tagami, U.; Okamoto, N. One-Step Construction of Ferritin Encapsulation Drugs for Cancer Chemotherapy. *Nanoscale* **2021**, *13* (3), 1875−1883.
(19) Tetter, S.; Hilvert, D. Enzyme Encapsulation by a Ferritin Cage. *Angew. Chem., Int. Ed.* **2017**, *56* (47), 14933−14936.
(20) Pontillo, N.; Pane, F.; Messori, L.; Amoresano, A.; Merlino, A. Cisplatin Encapsulation within a Ferritin Nanocage: A High-Resolution Crystallographic Study. *Chem. Commun.* **2016**, *52* (22), 4136−4139.
(21) Cheng, X.; Xie, Q.; Sun, Y. Advances in Nanomaterial-Based Targeted Drug Delivery Systems. *Front. Bioeng. Biotechnol.* **2023**, *11*, 1177151.
(22) Kawabata, H. Transferrin and Transferrin Receptors Update. *Free Radical Biol. Med.* **2019**, *133*, 46−54.
(23) Gammella, E.; Buratti, P.; Cairo, G.; Recalcati, S. The Transferrin Receptor: The Cellular Iron Gate. *Metallomics* **2017**, *9* (10), 1367−1375.
(24) Shen, Y.; Li, X.; Dong, D.; Zhang, B.; Xue, Y.; Shang, P. Transferrin Receptor 1 in Cancer: A New Sight for Cancer Therapy. *Am. J. Cancer Res.* **2018**, *8* (6), 916−931.
(25) Li, L.; Fang, C. J.; Ryan, J. C.; Niemi, E. C.; Lebrón, J. A.; Björkman, P. J.; Arase, H.; Torti, F. M.; Torti, S. V.; Nakamura, M. C.; Seaman, W. E. Binding and Uptake of H-Ferritin Are Mediated by Human Transferrin Receptor-1. *Proc. Natl. Acad. Sci. U. S. A.* **2010**, *107* (8), 3505−3510.
(26) Fan, K.; Cao, C.; Pan, Y.; Lu, D.; Yang, D.; Feng, J.; Song, L.; Liang, M.; Yan, X. Magnetoferritin Nanoparticles for Targeting and Visualizing Tumour Tissues. *Nat. Nanotechnol.* **2012**, *7* (7), 459−464.
(27) Bouzinab, K.; Summers, H. S.; Stevens, M. F. G.; Moody, C. J.; Thomas, N. R.; Gershkovich, P.; Weston, N.; Ashford, M. B.; Bradshaw, T. D.; Turyanska, L. Delivery of Temozolomide and N3-Propargyl Analog to Brain Tumors Using an Apoferritin Nanocage. *ACS Appl. Mater. Interfaces* **2020**, *12* (11), 12609−12617.
(28) Abuzaid, H.; Abdelrazig, S.; Ferreira, L.; Collins, H. M.; Kim, D.-H.; Lim, K.-H.; Kam, T.-S.; Turyanska, L.; Bradshaw, T. D. Apoferritin-Encapsulated Jerantinine A for Transferrin Receptor Targeting and Enhanced Selectivity in Breast Cancer Therapy. *ACS Omega* **2022**, *7* (25), 21473−21482.
(29) Zhen, Z.; Tang, W.; Guo, C.; Chen, H.; Lin, X.; Liu, G.; Fei, B.; Chen, X.; Xu, B.; Xie, J. Ferritin Nanocages To Encapsulate and Deliver Photosensitizers for Efficient Photodynamic Therapy against Cancer. *ACS Nano* **2013**, *7* (8), 6988−6996.
(30) Wang, W.; Wang, L.; Li, G.; Zhao, G.; Zhao, X.; Wang, H. AB Loop Engineered Ferritin Nanocages for Drug Loading under Benign Experimental Conditions. *Chem. Commun.* **2019**, *55* (82), 12344−12347.
(31) Chen, H.; Zhang, S.; Xu, C.; Zhao, G. Engineering Protein Interfaces Yields Ferritin Disassembly and Reassembly under Benign Experimental Conditions. *Chem. Commun.* **2016**, *52* (46), 7402−7405.
(32) Zhang, J.; Cheng, D.; He, J.; Hong, J.; Yuan, C.; Liang, M. Cargo Loading within Ferritin Nanocages in Preparation for Tumor-Targeted Delivery. *Nat. Protoc.* **2021**, *16* (10), 4878−4896.
(33) Shu, X.; Lev-Ram, V.; Deerinck, T. J.; Qi, Y.; Ramko, E. B.; Davidson, M. W.; Jin, Y.; Ellisman, M. H.; Tsien, R. Y. A Genetically Encoded Tag for Correlated Light and Electron Microscopy of Intact Cells, Tissues, and Organisms. *PloS Biol.* **2011**, *9* (4), No. e1001041.
(34) Westberg, M.; Holmegaard, L.; Pimenta, F. M.; Etzerodt, M.; Ogilby, P. R. Rational Design of an Efficient, Genetically Encodable, Protein-Encased Singlet Oxygen Photosensitizer. *J. Am. Chem. Soc.* **2015**, *137* (4), 1632−1642.
(35) Kaya, S. G.; Hovan, A.; Fraaije, M. W. Engineering of LOV-Domains for Their Use as Protein Tags. *Arch. Biochem. Biophys.* **2025**, *763*, 110228.
(36) Diaz, D.; Vidal, X.; Sunna, A.; Care, A. Bioengineering a Light-Responsive Encapsulin Nanoreactor: A Potential Tool for In Vitro Photodynamic Therapy. *ACS Appl. Mater. Interfaces* **2021**, *13* (7), 7977−7986.
(37) Ruiz-González, R.; Cortajarena, A. L.; Mejias, S. H.; Agut, M.; Nonell, S.; Flors, C. Singlet Oxygen Generation by the Genetically Encoded Tag MiniSOG. *J. Am. Chem. Soc.* **2013**, *135* (26), 9564−9567.
(38) Ingenbosch, K. N.; Quint, S.; Dyllick-Brenzinger, M.; Wunschik, D. S.; Kiebist, J.; Süss, P.; Liebelt, U.; Zuhse, R.; Menyes, U.; Scheibner, K.; Mayer, C.; Opwis, K.; Gutmann, J. S.; Hoffmann-Jacobsen, K. Singlet-Oxygen Generation by Peroxidases and Peroxygenases for Chemoenzymatic Synthesis. *ChemBiochem* **2021**, *22* (2), 398−407.
(39) Rabello, B. R.; Gerola, A. P.; Pellosi, D. S.; Tessaro, A. L.; Aparício, J. L.; Caetano, W.; Hioka, N. Singlet Oxygen Dosimetry Using Uric Acid as a Chemical Probe: Systematic Evaluation. *J. Photochem. Photobiol. A Chem.* **2012**, *238*, 53−62.
(40) Torra, J.; Lafaye, C.; Signor, L.; Aumonier, S.; Flors, C.; Shu, X.; Nonell, S.; Gotthard, G.; Royant, A. Tailing MiniSOG: Structural Bases of the Complex Photophysics of a Flavin-Binding Singlet Oxygen Photosensitizing Protein. *Sci. Rep.* **2019**, *9* (1), 2428.
(41) Pediconi, N.; Ghirga, F.; Del Plato, C.; Peruzzi, G.; Athanassopoulos, C. M.; Mori, M.; Crestoni, M. E.; Corinti, D.; Ugozzoli, F.; Massera, C.; Arcovito, A.; Botta, B.; Boffi, A.; Quaglio, D.; Baiocco, P. Design and Synthesis of Piperazine-Based Compounds Conjugated to Humanized Ferritin as Delivery System of SiRNA in Cancer Cells. *Bioconjugate Chem.* **2021**, *32* (6), 1105−1116.
(42) Shilova, O. N.; Proshkina, G. M.; Ryabova, A. V.; Deyev, S. M. Anti-HER2 Phototoxin Based on Flavoprotein MiniSOG Causes the Oxidative Stress and Necrosis of HER2-Positive Cancer Cells. *Moscow Univ. Biol. Sci. Bull.* **2016**, *71* (1), 14−18.
(43) Ryumina, A. P.; Serebrovskaya, E. O.; Staroverov, D. B.; Zlobovskaya, O. A.; Shcheglov, A. S.; Lukyanov, S. A.; Lukyanov, K. A. Lysosome-Associated MiniSOG as a Photosensitizer for Mammalian Cells. *BioTechniques* **2016**, *61* (2), 92−94.
(44) Hoffmann, S.; Orlando, M.; Andrzejak, E.; Bruns, C.; Trimbuch, T.; Rosenmund, C.; Garner, C. C.; Ackermann, F. Light-Activated ROS Production Induces Synaptic Autophagy. *J. Neurosci.* **2019**, *39* (12), 2163.
(45) Kim, M. M.; Darafsheh, A. Light Sources and Dosimetry Techniques for Photodynamic Therapy. *Photochem. Photobiol.* **2020**, *96* (2), 280−294.
(46) Zhang, Y.; Zheng, J.; Jin, F.; Xiao, J.; Lan, N.; Xu, Z.; Yue, X.; Li, Z.; Li, C.; Cao, D.; Wang, Y.; Zhong, W.; Ran, Y.; Guan, B.-O. Fiber-Optic Drug Delivery Strategy for Synergistic Cancer Photothermal-Chemotherapy. *Light: sci. Appl.* **2024**, *13* (1), 228.

https://doi.org/10.1021/acsabm.5c00098
ACS Appl. Bio Mater. 2025, 8, 3909−3919